The KW-Boundary Hybrid Digital Waveguide Mesh for Room Acoustics Applications

Damian T. Murphy and Mark Beeson

Abstract—**The digital waveguide mesh is a discrete-time simulation used to model acoustic wave propagation through a bounded medium. It can be applied to the simulation of the acoustics of rooms through the generation of impulse responses suitable for auralization purposes. However, large-scale three-dimensional mesh structures are required for high quality results. These structures must therefore be efficient and also capable of flexible boundary implementation in terms of both geometrical layout and the possibility for improved mesh termination algorithms. The general one-dimensional N-port boundary termination is investigated, where N depends on the geometry of the modeled domain and the mesh topology used. The equivalence between physical variable Kirchoff-model, and scattering-based wave-model boundary formulations is proved. This leads to the KW-hybrid one-dimensional N-port boundary-node termination, which is shown to be equivalent to the Kirchoff- and wave-model cases. The KW-hybrid boundary-node is implemented as part of a new hybrid two-dimensional triangular digital waveguide mesh. This is shown to offer the possibility for large-scale, computationally efficient mesh structures for more complex shapes. It proves more accurate than a similar rectilinear mesh in terms of geometrical fit, and offers significant savings in processing time and memory use over a standard wave-based model. The new hybrid mesh also has the potential for improved real-world room boundary simulations through the inclusion of additional mixed modeling algorithms.**

Index Terms—**Acoustic propagation, acoustic signal processing, digital waveguides, finite-difference time-domain (FDTD) methods, multidimensional systems.**

I. INTRODUCTION

THE digital waveguide mesh (DWM) [1] is a discrete-time simulation used to model acoustic wave propagation in an enclosed system that has been shown to be appropriate for virtual acoustic applications through the generation of room impulse responses (RIRs) suitable for auralization purposes [2], [3]. Most current RIR generation methods are based on geometric acoustic techniques [4], [5], although these methods are valid for high frequencies only and less appropriate for low frequencies where the presence of sparsely distributed modal frequencies tends to dominate. Geometric models are further limited in their ability to successfully model indirect sound paths caused by diffraction, a fundamental property when

considering building interiors or city plans, where the direct line of sight between sound source and listener is often blocked. Diffraction can be implemented as part of such a model by considering incident–sound/object–edge collisions as additional secondary sources according to, for instance, the Uniform Theory of Diffraction as applied to geometrical acoustics, but at additional computational cost. However real-time implementation for certain types of interactive sound environments has met with some success [6], allowing occluded sound sources to be spatially localized, hence, demonstrating the importance of including diffraction effects as part of an accurate auralization model.

Finite-element and boundary-element models offer alternative methods for calculating modal frequencies present within an enclosed space and have been used to create RIRs of virtual rooms [7]. However, the DWM produces equally valid results with less computational overhead and greater flexibility in terms of implementation and realization. Although computationally intensive for large spaces, wave propagation effects such as diffraction are an inherent part of the implementation [3], requiring no additional processing load.

The DWM is an extension of the one-dimensional (1-D) digital waveguide commonly used to model string and wind instruments [8], an approach similar to the Kelly–Lochbaum 1-D transmission line simulation of the vocal tract [9]. Both of these 1-D models are based on a sampled traveling-wave implementation of the d'Alembert solution to the wave equation using bidirectional digital delay lines and scattering junctions. Digital waveguide models therefore result in the propagation of a physical quantity through its division into two directional wave components and schemes implemented in this way are termed *W-models* [10], [11]. Hence, the term W-DWM is used to describe a DWM similarly based on a sampled traveling-wave solution. A linear transformation of a W-DWM leads to an alternative implementation as a K-variable DWM (K-DWM), depending on physical quantities only rather than sampled traveling-wave components. Such *K-models* [10], [11] are named after the Kirchoff type physical variables used. In this form, and under certain conditions, a K-DWM can be computationally equivalent to a finite-difference time-domain (FDTD) simulation. Recent work has explored the equivalence between K- and W-models [10], [12]. The K-DWM and FDTD approaches are computationally efficient in terms of memory and processing time, whereas the scattering-based W-DWM implementation leads to more flexible boundary termination options for complex geometries. The ability to deal with nontrivial boundary geometries together with the minimization of processing resources are important requirements for high quality virtual space RIR generation.

The authors are with The Intelligent Systems Group-Audio Lab, Department of Electronics, University of York, York YO10 5DD U.K. (e-mail: dtm3@ohm.york.ac.uk; mjb128@ohm.york.ac.uk).

Mixed modeling scenarios where K-DWM and W-DWM approaches have been interfaced in 1-D via a KW-pipe have been proposed in [11], leading to the formulation of a two-dimensional (2-D) hybrid DWM [10], the properties of which have been explored in [13]. The 2-D hybrid mesh combines the computational efficiency of the K-DWM approach with the flexibility of scattering-based boundaries through the use of KW-pipes. Its validation and implementation is the subject of this paper.

The work in [10] showed the functional equivalence between W-DWM and K-DWM approaches and how mixed models could be constructed using KW-pipes. One suggested example is the 2-D hybrid digital waveguide mesh. This paper examines the special case of the generalized 1-D termination of an N-port boundary-node, not explicitly covered in [10] and leads to the contributions of this paper. A general 1-D termination of an N-port boundary-node is shown to have equivalent K-DWM and W-DWM boundary formulations. From this result, the KW-hybrid 1-D termination of an N-port boundary-node is introduced and similarly shown to be equivalent to the K-DWM and W-DWM cases. This potentially leads to new families of efficient hybrid DWM models beyond those presented previously, that are able to deal with nontrivial geometrical structures, and make use of other computational possibilities in terms of boundary termination. In particular, this paper examines how the presented KW-hybrid boundary-node can be applied in a new 2-D triangular hybrid-DWM, and explores some of the improvements in accuracy and computational savings offered.

This paper is organized as follows. Section II presents an overview of the general DWM and a discussion of the factors that currently limit this method for virtual acoustics applications. Section III reviews previous methods for 1-D boundary termination, examines the basic 1-D, 2-port boundary, and discusses how it can be extended to deal with more complex arbitrary geometries through the enhanced connectivity options offered by the 2-D triangular W-DWM. This section goes on to consider the general 1-D termination of an N-port boundary for the W-DWM case, shows the equivalence of the K-DWM case, and proposes the new KW-hybrid 1-D termination. This KW-hybrid boundary-node is then shown to be equivalent to the general W-DWM/K-DWM case. In Section IV, this new boundary-node formulation is applied in the 2-D triangular DWM for test case scenarios appropriate to the field of virtual room acoustics, demonstrating how it improves upon the basic rectilinear 2-D DWM, while offering comparable results and significant computational savings over the triangular 2-D W-DWM.

II. DIGITAL WAVEGUIDE MESH

A. Background

The digital waveguide mesh is derived from the 1-D digital waveguide used extensively for physical modeling synthesis. The reader is referred to [8] and [14] for a thorough treatment and discussion of this area and a full derivation of some of the equations that follow, which are presented here again for completeness. Higher dimension mesh structures are constructed
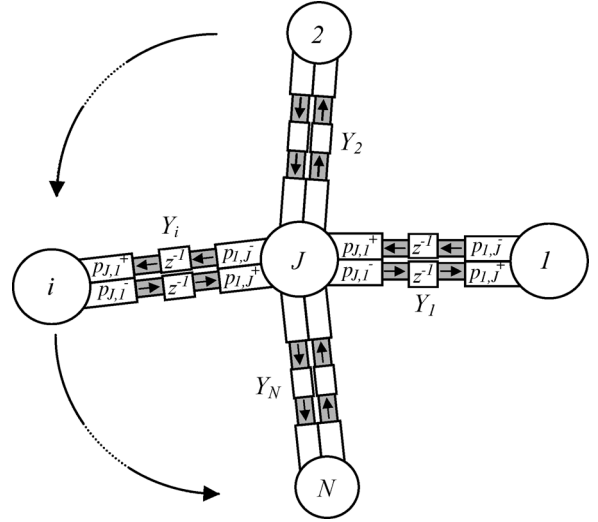

Fig. 1. General scattering junction J with N connected waveguides of admittance Y_i for $i = 1, 2, \ldots, N$.
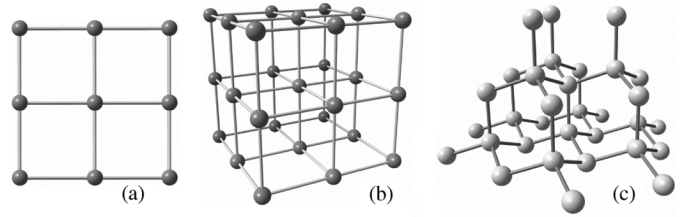

Fig. 2. (a) The 2-D rectilinear, (b) 3-D rectilinear, and (c) 3-D tetrahedral mesh.

using bidirectional delay lines and scattering junctions which act as spatial and temporal sampling points within the modeled space. The sound pressure in a waveguide is represented by p_i, the volume velocity by v_i, and the impedance of the waveguide by Z_i where $p_i/v_i = Z_i$. The admittance Y_i is the inverse of Z_i, such that $Y_i = 1/Z_i$. The input to a waveguide is termed p_i^+ and the output p_i^-. The signal $p_{J,i}^+$ therefore represents the incoming signal to junction J along the waveguide from the opposite junction i. Similarly, the signal $p_{J,i}^-$ represents the outgoing signal from junction J along the waveguide to the opposite junction i.

Fig. 1 shows the general case of a scattering junction J with N neighbors, $i = 1, 2, \ldots, N$, with each connected unit waveguide element having an associated admittance Y_i. Connecting delay lines together at scattering junctions in this manner allows spatial and temporal sampling grids to be defined that are analogous to the physical objects they are attempting to model. For instance, Fig. 2(a) shows the 2-D rectilinear waveguide mesh constructed from four-port scattering junctions. It is also possible to use different mesh topologies to model the same physical space. Figs. 2(b) and (c) show two such topologies—the 3-D rectilinear mesh and the tetrahedral mesh—both of which can be used to model wave propagation through a 3-D space.

The 1-D waveguide is a discretized formulation of the d'Alembert traveling wave solution to the 1-D wave equation

$$\frac{\partial^2 p(x,t)}{\partial t^2} = c^2 \frac{\partial^2 p(x,t)}{\partial x^2}. \tag{1}$$

This can be implemented using two bidirectional delay lines as shown in Fig. 1 and so the sound pressure of a propagating wave signal can be defined as the sum of these traveling waves or alternatively the input and output of this waveguide element

$$p_{J,i} = p_{J,i}^+ + p_{J,i}^-. \tag{2}$$

By determining that for a lossless junction J the sum of the input velocities is equal to the sum of the output velocities, and that the sound pressures in all crossing waveguides are equal, the sound pressure p_J at junction J for N connected waveguides can be expressed as

$$p_J = \frac{2 \sum_{i=1}^{N} Y_i \cdot p_{J,i}^+}{\sum_{i=1}^{N} Y_i}. \tag{3}$$

As the waveguides are equivalent to bidirectional unit-delay lines, the input to scattering junction J at time index n, $p_{J,i}^+(n)$, is equal to the output from neighboring junction i into the connecting waveguide at the previous time step $p_{i,J}^-(n-1)$. Expressing this relationship in the z-domain gives

$$p_{J,i}^+ = z^{-1} \cdot p_{i,J}^-. \tag{4}$$

Equations (2)–(4) are termed the scattering equations for the mesh structure. Continuing with this z-transform notation, and using (2)–(4) it is also possible to derive the equivalent K-variable formulation for these lossless scattering equations in terms of junction pressure values only

$$p_J = \frac{2}{N} \sum_{i=1}^{N} p_i \cdot z^{-1} - p_J \cdot z^{-2}. \tag{5}$$

Note that (5) holds for homogeneous media only, as this derivation assumes all admittances are equal. Note also that (5) can be derived directly from a finite-difference formulation of the 2-D case of the wave equation in (1). The W-DWM scattering equations or K-DWM formulation can be used to implement a range of topologies/structures from simple 1-D strings or air columns [15], 2-D triangular and rectilinear-based plates or membranes [16], through to three-dimensional (3-D) rectilinear [17], tetrahedral [18], and dodecahedral structures [19]. There is also another important family of DWMs based on an interpolated rectilinear mesh structure in either 2-D [20] or 3-D [21]. Interpolated DWMs demonstrate wave propagation characteristics approaching that of triangular/dodecahedral topologies but without the additional computational expense of a denser and more complex structure.

Typically, the term *DWM* has been previously used to describe both classes of model implementation. Such naming conventions are continued in this paper, with DWM being used to refer to the general class unless it is otherwise replaced by the use of the *K-DWM or W-DWM* descriptor.

B. Mesh Limitations

There are a number of factors that currently limit DWM models as an optimal solution for full virtual acoustic applications. The first is dispersion error, where the velocity of the propagating wave is dependent upon both its frequency and direction of travel, leading to wave propagation errors and a mistuning of the expected resonant modes. The degree of dispersion error is highly dependent upon mesh topology and has been investigated in [18]. Both the interpolated and triangular DWMs demonstrate dispersion characteristics that are substantially reduced to a function of frequency only, with frequency warping techniques [20], [21] giving further significant improvements. Oversampling the mesh also offers improvements in this regard, such that the required bandwidth lies within accepted limits, typically $0.25 \times f_{\text{update}}$ [1], where f_{update} is given by

$$f_{\text{update}} = \frac{c\sqrt{D}}{d} \tag{6}$$

where c is the speed of sound, D is the dimension of the mesh, and d is the spatial distance between mesh junctions. Ultimately, f_{update} will dictate the quality of RIR output from the mesh with large sample rates requiring exponentially denser meshes, more computer memory, and hence taking longer to run, limiting this method to offline generation of RIRs only. Current work also involves the development of DWM models that can deal with frequency and direction dependent reflection at a boundary together with the incorporation of diffusion effects [22], [23].

III. KW-BOUNDARY HYBRID MESH

A. One-Dimensional Boundary Termination

A number of possibilities have been explored for terminating a DWM at a boundary. In [24], a 10×10 node 2-D rectilinear DWM is terminated with single one-pole allpass filters around the boundary, which may be interpreted as a 1-D termination connected to an ideal spring. This boundary implementation allows modal frequencies in the DWM to be retuned appropriately.

For curved boundaries, where the perimeter of the structure being modeled (such as a drum membrane) is not normal/parallel to the axes of the mesh structure, *rimguides* have been suggested as an appropriate solution [25]. Rimguides are noninteger length waveguide elements, comprising an integer length waveguide and a first-order allpass filter to model the fractional part. This method has been shown to be appropriate for modeling circular membranes using a triangular mesh at low frequencies, but becomes less accurate with increasing frequency. However, this is most likely due to the frequency-dependent dispersion characteristics of the triangular mesh.

In [26], 1-D termination incorporating 2-port boundary-nodes and a reflection factor based on a change in admittance of connected waveguide elements is extended to three- and four-port boundary-node cases for a triangular DWM (note that a similar approach is used in the following). Digital waveguide filters are used to process reflections from each connection individually, leading to a more accurate positioning of resonant modes in a 2-D rectangular membrane.

In room acoustics applications [2], [27], a DWM is often most simply terminated at a boundary via a 1-D connection as shown in Fig. 3. A boundary in a real room will act to reflect an incident sound wave, usually with some frequency-dependent absorption
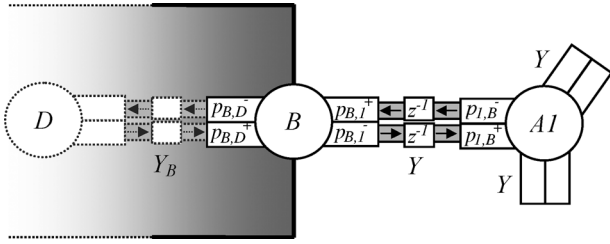
Fig. 3. Digital waveguide mesh termination at a boundary via a 1-D connection between boundary-node B and air-node A1.

Fig. 4. Rectilinear and triangular DWM representations of the same 2-D geometry. The six-port triangular mesh has the potential for more boundary-node types and so offers more connectivity options than the rectilinear case.

of the wave energy at the boundary itself. In a DWM a reflection is caused by a change in the admittance of different waveguide elements connected at a scattering junction [2]. The simplest case can be considered by connecting a dummy junction on the other side of the boundary junction, essentially within the boundary itself as in Fig. 3. The dummy junction is connected to the boundary junction (or boundary-node) via a waveguide element of admittance Y_B. The boundary-node in turn is connected to a single N-port scattering junction in the main body of the mesh (an air-node) with a waveguide element of admittance Y that is common to all lossless homogeneous waveguide elements in the structure. Therefore, if at such a boundary there is a change in admittance from Y to Y_B the reflection coefficient r is defined as

$$r = \frac{Y - Y_B}{Y + Y_B} \qquad (7)$$

where $0 \leq r \leq 1$. If $Y_B = yY$ for $0 \leq y \leq 1$, then

$$y = \frac{1-r}{1+r}. \qquad (8)$$

Given that there is no contribution into the boundary-node B from the dummy junction D, and using (3), the sound pressure for the boundary-node can be calculated as a function of the sound pressures of the incident traveling waves

$$p_B = (1+r) \cdot p_{B,1}^+. \qquad (9)$$

The equivalent K-DWM boundary, as presented in [27] is given by

$$p_B = (1+r)p_1 \cdot z^{-1} - r \cdot p_B \cdot z^{-2}. \qquad (10)$$

A full derivation of (10) is offered in the Appendix. The amount of energy reflected at the boundary is determined by setting r equal to a value between 0 and 1, with $r = 1$ giving total reflection and $r = 0$ approximating anechoic conditions.

Other improvements to this DWM boundary-node derivation have also been suggested. In [28], the boundary-node in Fig. 3 is replaced with a boundary filter with transfer function $H(z)$. This transfer function is defined to optimally match given frequency dependent reflection coefficient data for a particular material, and implemented using a first-order IIR filter for a 2-D K-DWM
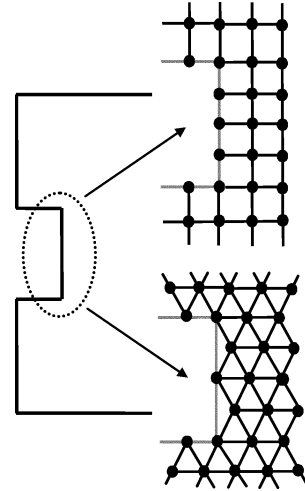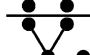
TABLE I
2-D TRIANGULAR MESH BOUNDARY TYPES

Boundary Type	Connected Air Nodes	W-DWM Scattering Equation
	1	$p_B = (1+r) \cdot p_{B,1}^{+}$
	2	$p_B = \frac{2(1+r)}{3+r} \sum_{i=1}^{2} p_{B,i}^{+}$
	3	$p_B = \frac{1+r}{2+r} \sum_{i=2}^{4} p_{B,i}^{+}$
	4	$p_B = \frac{2(1+r)}{5+3r} \sum_{i=1}^{4} p_{B,i}^{+}$
	5 - no boundary connection	$p_B = \frac{2}{5} \sum_{i=1}^{5} p_{B,i}^{+}$
	5	$p_B = \frac{1+r}{3+2r} \sum_{i=1}^{5} p_{B,i}^{+}$

rectilinear mesh structure. The results given are a good approximation to the required target responses, but are subject to the directional dependent characteristics of the mesh structure itself, being less accurate for certain angles of incidence.

Fig. 4 shows an example of two mesh structures used to model a simple 2-D geometry using both the rectilinear and triangular mesh topologies. Note that with the rectilinear mesh, most boundary-nodes consist of a connection to a single air-node, whereas with the triangular mesh there are a number of different possibilities with a single boundary-node having multiple connections to two, three, or four air-nodes. By extending the basic single air-node case as discussed above, it is possible to derive the scattering equations for all possible boundary types when using the 2-D triangular DWM. For instance, in the case of a boundary-node connected to two air-nodes, there are a total of three junction connections, with one being to the dummy junction D which again has no contribution into the boundary-node itself. The pressure value at the

Fig. 5. (a) General 1-D termination of an N-port W-DWM boundary-node B connected to an $M + 1$ port W-DWM air-node A1 in functional block diagram form. (b) Equivalent functional block diagram for the K-DWM boundary-node/air-node connection.

boundary-node can then be calculated using (3) with $N = 3$. The change in admittance is characterized using (8) leading to an expression in terms of the reflection factor r only. The other cases can be derived similarly and are summarized in Table I.
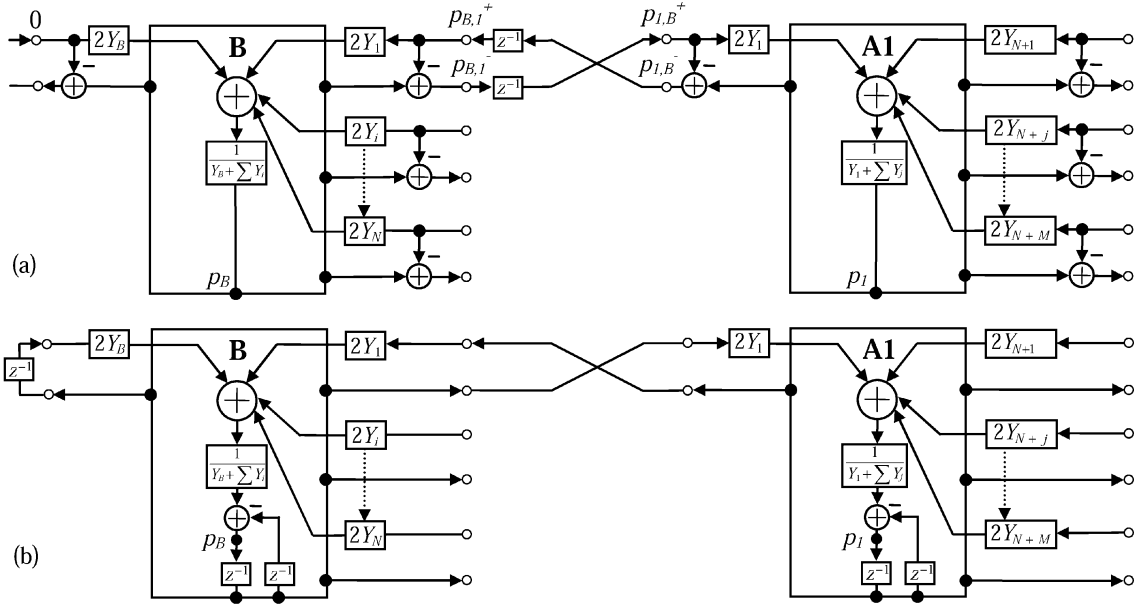
It has already been stated that the 2-D triangular DWM is the favored noninterpolated mesh topology for minimizing direction-dependent dispersion. An additional benefit with this mesh structure can now be seen in the increased connection possibilities at a boundary. If a particular nonrectangular 2-D complex geometry is required to be modeled, the triangular DWM will provide a closer fit to the defined boundary than a similar rectilinear-based mesh due to the enhanced connectivity offered by the six-port scattering junction that forms the basis of this model.

What follows is a more considered examination of the multiport 1-D boundary-node termination for the W-DWM case, and how the enhanced connectivity it offers can be equivalently applied in the K-DWM and hybrid/mixed modeling cases.

B. Signal Behavior at a 1-D Boundary Termination

A rigorous approach to the compatibility and equivalence of K-, W-, and mixed modeling structures has been presented and applied in [10]. This result concluded that these cases are functionally equivalent across any common topology and parametric value. A similar method adapted for purpose is applied here for the particular case of an N-port boundary-node 1-D termination, as might be used in a typical DWM.

Fig. 5(a) presents the general 1-D termination of an N-port boundary-node B connected to a single $M + 1$ port air-node A1 in functional block diagram form. This can be considered as an extension of Fig. 3 to the general case. The scattering junction on the left is the boundary-node B terminated with a 1-D connection of admittance Y_B (equivalent to an infinitely long connection of admittance-matched unit delay lines, implying that

there is no contribution back into the junction, hence zero input at this terminal) and with up to N other connecting terminals (where, for example, with the 2-D triangular mesh, $N = 5$). One such air-node, A1, is shown connected via a waveguide element of admittance Y_1 and with up to M other connecting terminals (where again $M = 5$ in the 2-D triangular mesh case). Incoming and outgoing pressure signals between boundary-node B and air-node A1 have been labeled appropriately and the pressure value at each is given by p_B and p_1, respectively.

Fig. 5(b) shows the equivalent K-DWM boundary. Note that the main difference between the two formulations is that the W-DWM has memory located in the bidirectional unit delay lines, whereas the K-DWM has two unit delays of internal memory within the actual junction and delay-free connections between nodes. The 1-D connection of admittance Y_B is in this case equivalently terminated as a feedback loop with unit delay [10].

Equivalence for the K-, W-, and mixed modeling implementations of this general 1-D boundary termination is established first by examining a typical direct connection between a boundary-node and an air-node for both the W-DWM and K-DWM cases. From Fig. 5(a), the junction pressure values for p_B and p_1 are determined in terms of admittance values Y_i and Y_{N+j} and incoming W-variables $p_{B,i}^+$ and $p_{1,N+j}^+$, respectively. Note that it is assumed that the connecting terminals with associated admittances, Y_i and Y_{N+j}, not explicitly considered as part of the diagram, are numbered similarly. These W-DWM expressions for p_B and p_1 are then linearly transformed to be dependent on physical K-variables only. From Fig. 5(b), the junction pressure values for p_B and p_1 are determined directly for the K-DWM case and shown to be equivalent to the K-variable transformed W-DWM example.

Consider first the case of the $M + 1$ port air-node, A1, in a W-DWM, and let A1 be connected directly to an N-port

boundary-node B. From Fig. 5(a), p_1 can be expressed in terms of incoming W-variables $p_{1,N+j}^+$

$$p_1 = \frac{2Y_1 \cdot p_{1,B}^+ + 2 \cdot \sum_{j=1}^{M} Y_{N+j} \cdot p_{1,N+j}^+}{Y_1 + \sum_{j=1}^{M} Y_{N+j}}$$

$$= \frac{2Y_1 \cdot p_{B,1}^- \cdot z^{-1} + 2 \cdot \sum_{j=1}^{M} Y_{N+j} \cdot p_{N+j,1}^- \cdot z^{-1}}{Y_1 + \sum_{j=1}^{M} Y_{N+j}} \quad (11)$$

$$p_{1,B}^- = p_1 - p_{B,1}^- \cdot z^{-1} \quad (12)$$

$$p_{B,1}^- = p_B - p_{1,B}^- \cdot z^{-1}. \quad (13)$$

Substituting (13) in (12) gives

$$p_{1,B}^- = \frac{p_1 - p_B \cdot z^{-1}}{1 - z^{-2}} \quad (14)$$

and similarly, substituting (12) in (13) gives

$$p_{B,1}^- = \frac{p_B - p_1 \cdot z^{-1}}{1 - z^{-2}}. \quad (15)$$

Transformations similar to (14) and (15) exist for the general terms $p_{N+j,1}^-$ and $p_{1,N+j}^-$, and in the case of boundary-node B, $p_{B,i}^-$ and $p_{i,B}^-$. Note that in certain cases, connecting terminals for A1 and B will share a common air-node and, hence, the scenario arises where $p_i = p_{N+j}$, although this possibility does not have any impact on the derivations that follow. Substituting (15) and the corresponding expression for $p_{N+j,1}^-$ in (11) eliminates the wave variables leaving p_1 in terms of physical K-variables only

$$p_1 = \frac{1}{Y_1 + \sum_{j=1}^{M} Y_{N+j}} 2 \cdot Y_1 \cdot \left[\frac{(p_B - p_1 \cdot z^{-1})}{1 - z^{-2}} \right] \cdot z^{-1}$$

$$+ \frac{1}{Y_1 + \sum_{j=1}^{M} Y_{N+j}} 2 \cdot \sum_{j=1}^{M} Y_{N+j} \cdot \left[\frac{(p_{N+j} - p_1 \cdot z^{-1})}{1 - z^{-2}} \right] \cdot z^{-1}. \quad (16)$$

Solving (16) for p_1

$$p_1 = \frac{2 \cdot \left(Y_1 \cdot p_B + \sum_{j=1}^{M} Y_{N+j} \cdot p_{N+j} \right) \cdot z^{-1}}{\left(Y_1 + \sum_{j=1}^{M} Y_{N+j} \right) \cdot (1 + z^{-2})}. \quad (17)$$

Let admittances Y_j be set such that they are equal to the admittance Y_1 connecting B and A1, as would be the case for a wider homogenous DWM system. Therefore, (17) becomes

$$p_1 = \frac{2 \cdot \left(p_B + M \cdot \sum_{j=1}^{M} p_{N+j} \right) \cdot z^{-1}}{(1 + M) \cdot (1 + z^{-2})}. \quad (18)$$

Therefore, (18) is the expression for an $M + 1$ port homogeneous W-DWM air-node, transformed to the physical K-variable case. If $M = 3$ and noting that p_B can also be considered as any general input signal, (18) is equivalent to (5), the K-variable formulation of the lossless scattering equations for a homogeneous 2-D rectilinear DWM. Considering boundary-node B, from Fig. 5(a), p_B can be expressed in terms of incoming W-variables $p_{B,i}+$

$$p_B = \frac{2 \cdot \sum_{i=1}^{N} Y_i \cdot p_{B,i}^+}{Y_B + \sum_{i=1}^{N} Y_i}$$

$$= \frac{2 \cdot \sum_{i=1}^{N} Y_i \cdot p_{i,B}^- \cdot z^{-1}}{Y_B + \sum_{i=1}^{N} Y_i}. \quad (19)$$

Eliminating wave variables $p_{i,B}^-$ by substituting the general form of (14) expressed in terms of i in (19) leaves p_B in terms of physical K-variables only

$$p_B = \frac{1}{Y_B + \sum_{i=1}^{N} Y_i} \cdot 2 \cdot \sum_{i=1}^{N} Y_i \cdot \left[\frac{(p_i - p_B \cdot z^{-1})}{1 - z^{-2}} \right] \cdot z^{-1}. \quad (20)$$

Solving (20) for p_B

$$p_B = \frac{2 \cdot \left(\sum_{i=1}^{N} Y_i \cdot p_i \right) \cdot z^{-1}}{\left(Y_B + \sum_{i=1}^{N} Y_i \right) - \left(Y_B - \sum_{i=1}^{N} Y_i \right) \cdot z^{-2}}. \quad (21)$$

In the case of a boundary-node connected to an air-node in an otherwise homogeneous DWM system, with all admittances Y_i set such that they are equal to the admittance Y_1, the change in admittance at the boundary implies that $Y_B = yY_1$ for $0 \le y \le 1$, where y is defined as in (8). Therefore, (21) becomes

$$p_B = \frac{2 \cdot N \cdot p_i \cdot z^{-1}}{(y + N) - (y - N) \cdot z^{-2}} \quad (22)$$

and substituting (8) in (22) gives

$$p_B = \frac{2 \cdot N \cdot (1 + r) \cdot p_i \cdot z^{-1}}{N \cdot (1 + r) + 1 - r - [1 - r - N \cdot (1 + r)] \cdot z^{-2}}. \quad (23)$$

Therefore, (23) is the expression for an N-port homogeneous W-DWM boundary-node, transformed to the physical K-variable case. If $N = 1$, (23) is equivalent to (10), the K-DWM 1-D boundary-node termination condition as presented in Section III-A, which is in turn equivalent to the W-DWM case as given in (9). This result also provides an alternative to the previously used K-DWM derivation provided in the Appendix.

Fig. 5(b) is the block diagram for the K-DWM boundary, functionally equivalent to the W-DWM case presented in Fig. 5(a). Consider first the case of the $M + 1$ port K-DWM air-node A1 connected directly to N-port boundary-node B.
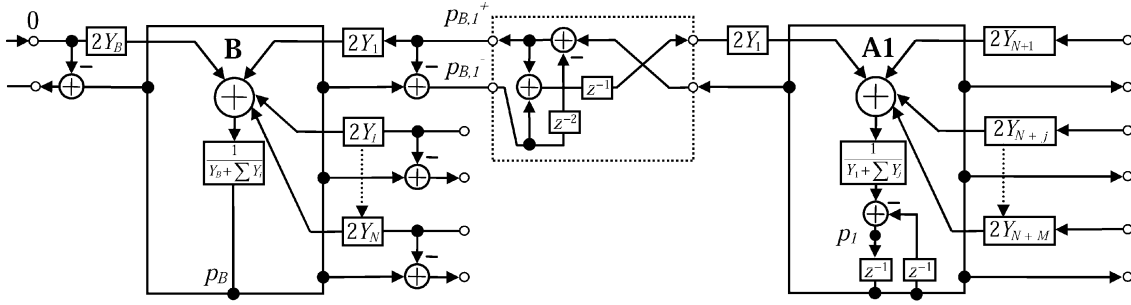
Fig. 6. Functional block diagram form of a KW-hybrid boundary-node to air-node 1-D termination. A K-variable air-node A1 is interfaced with a W-variable boundary-node B via a KW-pipe.

From Fig. 5(b), p_1 can be expressed in terms of neighboring K-variables p_{N+j}

$$p_1 = \frac{2 \cdot Y_1 \cdot p_B \cdot z^{-1}}{Y_1 + \sum_{j=1}^{M} Y_{N+j}} - p_1 \cdot z^{-2} + \frac{2 \cdot \sum_{j=1}^{M} Y_{N+j} \cdot p_{N+j} \cdot z^{-1}}{Y_1 + \sum_{j=1}^{M} Y_{N+j}}. \tag{24}$$

Solving (24) for p_1

$$p_1 = \frac{2 \cdot \left(Y_1 \cdot p_B + \sum_{j=1}^{M} Y_{N+j} \cdot p_{N+j} \right) \cdot z^{-1}}{\left(Y_1 + \sum_{j=1}^{M} Y_{N+j} \right) \cdot (1 + z^{-2})}. \tag{25}$$

Note that (25) is equivalent to (17) and, hence, (18) follows directly. This demonstrates the equivalence between the W-DWM air-node, transformed to the physical K-variable case, and the K-DWM air-node as derived directly. Considering boundary-node B, from Fig. 5(b), p_B can be expressed in terms of K-variables p_i

$$p_B = \frac{2 \cdot \sum_{i=1}^{N} Y_i \cdot p_i \cdot z^{-1}}{Y_B + \sum_{i=1}^{N} Y_i} - p_B \cdot z^{-2} + \frac{2 \cdot Y_B \cdot p_B \cdot z^{-2}}{Y_B + \sum_{i=1}^{N} Y_i}. \tag{26}$$

Solving (26) for p_B

$$p_B = \frac{2 \cdot \left(\sum_{i=1}^{N} Y_i \cdot p_i \right) \cdot z^{-1}}{\left(Y_B + \sum_{i=1}^{N} Y_i \right) - \left(Y_B - \sum_{i=1}^{N} Y_i \right) \cdot z^{-2}}. \tag{27}$$

In the case of a boundary-node connected to an air-node in an otherwise homogeneous DWM system, with all admittances Y_i set such that they are equal to the admittance Y_1, the change in admittance at the boundary implies that if $Y_B = yY_1$ for $0 \leq y \leq 1$ where y is defined as in (8), (23) follows directly from (27), hence demonstrating the equivalence between the W-DWM boundary-node, transformed to the physical K-variable case, and the K-DWM boundary-node as derived directly.

It has, therefore, been shown that a general 1-D termination of an N-port boundary-node, with N depending on the geometry of the modeled domain, and DWM topology used, will have

equivalent K- and W-DWM formulations. In particular, it follows that without loss of generality, this equivalence holds for the 2-D triangular DWM.

C. KW-Boundary Hybrid Mesh

The two implementations commonly used in DWM simulations are either based on the W-DWM, defined by (2)–(4), or the K-DWM defined according to (5). As shown in Fig. 4 and presented in Table I, W-DWMs based on the triangular topology are able to provide a better fit at the boundary of a more complex geometric structure due to the larger number of possible air-node connections. However, W-DWMs based on the scattering equations are computationally more inefficient than the equivalent K-DWM, relying on two independent passes through each element in the mesh data structure and greater memory resources.

The equivalence between W-DWM and K-DWM N-port boundaries presented in Section III-B demonstrates that it is now similarly appropriate to use N-port boundary terminations in a K-DWM, offering significant improvements in terms of speed and efficiency and the advantages of a better fit at the boundary of a more complex geometry. However, W-DWM boundary-node terminations have a number of additional possible advantages. These include mesh termination via rimguides [25] or fractional delays [29], the use of wave digital filters, which are considered in W-modeling terms [10], for frequency dependent boundaries, and the introduction of variable diffusively reflecting boundary conditions [23]. Therefore, it would clearly be useful if the speed and efficiency of a K-DWM could be combined with the enhanced flexibility of a W-DWM. These two mesh types can be interfaced using the *KW-pipe* transform as introduced in 1-D in [11] and proposed for the 2-D rectilinear DWM in [10]. It is shown in functional block diagram form in Fig. 6.

The KW-pipe is an all-pass network that is delay-free when moving from K-node to W-node, and that introduces delay in the opposite direction from W-node to K-node, so allowing physical variable K-DWM models to be effectively connected to scattering W-DWM models. In the example DWMs presented in this paper, KW-pipes are incorporated and combined into the standard W-DWM boundary-node resulting in a new hybrid DWM, with Fig. 7 showing this for the 2-D rectilinear case. In this hybrid DWM, the W-DWM/KW-pipe boundary-nodes
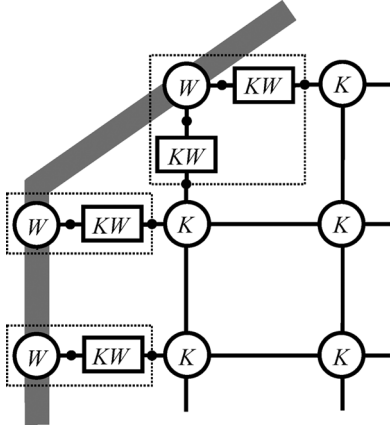
Fig. 7. New W-DWM boundary-nodes, in this case for the 2-D rectilinear mesh, incorporate KW-pipe connections to the main body of the mesh, giving them the external appearance of a standard K-DWM node.

offer additional possibilities in terms of geometrical and modeling flexibility, but are seen and managed by the DWM algorithm in the same way as standard K-DWM boundary-nodes. The air-nodes remain unaltered as regular K-DWM nodes and make up the overwhelming majority of the DWM simulation. The resulting hybrid model will, therefore, still benefit from the considerable improvements in terms of speed and memory of a purely K-DWM.

D. Signal Behavior at a 1-D KW-Pipe Termination

Now that the equivalence between K- and W-DWM formulations for a general 1-D termination of an N-port boundary-node has been established, as presented in Section III-B, it remains to be shown that this equivalence holds with the incorporation of a KW-pipe inserted between K-nodes and W-nodes in a DWM. In terms of implementation, a K-variable air-node should effectively "see" a connected W-variable boundary-node as any other standard K-variable node. Similarly, a W-variable boundary-node should "see" connections to neighboring K-variable air-nodes as being equivalent to a standard W-variable formulation.

Fig. 6 is the block diagram for the air-node/KW-pipe/boundary-node termination, functionally equivalent to the W-DWM and K-DWM cases presented in Fig. 5. Consider first the case for the $M+1$ port K-DWM air-node A1 connected directly to an N-port W-DWM boundary-node B via a KW-pipe (moving from K-DWM to W-DWM). From Fig. 6, p_1 can be expressed as follows:

$$p_1 = \frac{2 \cdot Y_1 \cdot \left(p_{B,1}^- - p_{B,1}^- \cdot z^{-2} + p_1 \cdot z^{-1}\right) \cdot z^{-1}}{Y_1 + \sum_{j=1}^{M} Y_{N+j}}$$

$$- p_1 \cdot z^{-2} + \frac{2 \cdot \sum_{j=1}^{M} Y_{N+j} \cdot p_{N+j} \cdot z^{-1}}{Y_1 + \sum_{j=1}^{M} Y_{N+j}}. \quad (28)$$

Eliminating wave variable $p_{B,1}^-$ by substituting (15) in (28) leaves p_1 in terms of physical K-variables only

$$p_1 = \frac{2 \cdot Y_1 \cdot p_B \cdot z^{-1}}{Y_1 + \sum_{j=1}^{M} Y_{N+j}} - p_1 \cdot z^{-2} + \frac{2 \cdot \sum_{j=1}^{M} Y_{N+j} \cdot p_{N+j} \cdot z^{-1}}{Y_1 + \sum_{j=1}^{M} Y_{N+j}}$$
$$(29)$$

which is the same form as (24) and, hence, (18) follows directly. Consider now the case for the N-port W-DWM boundary-node B connected directly to an N-port W-DWM air-node A1 via a KW-pipe (moving from W-DWM to K-DWM). From Fig. 6, p_B can be expressed as follows:

$$p_B = \frac{2 \cdot Y_1 \cdot p_{B,1}^+}{Y_B + \sum_{i=1}^{N} Y_i} + \frac{2 \cdot \sum_{i=2}^{N} Y_i \cdot p_{B,i}^+}{Y_B + \sum_{i=1}^{N} Y_i}$$

$$= \frac{2Y_1 \cdot \left(p_1 \cdot z^{-1} - p_{B,1}^- \cdot z^{-2}\right) \cdot z^{-1}}{Y_B + \sum_{i=1}^{N} Y_i}$$

$$+ \frac{2 \cdot \sum_{i=2}^{N} Y_i \cdot p_{i,B}^- \cdot z^{-1}}{Y_B + \sum_{i=1}^{N} Y_i} \quad (30)$$

Eliminating wave variables by substituting (15) and the corresponding expression for $p_{i,B}^-$ in (30) reduces p_B to an expression in terms of physical K-variables only

$$p_B = \frac{2 \cdot Y_1 \cdot \left(p_1 \cdot z^{-1} - p_B \cdot z^{-2}\right)}{Y_B + \sum_{i=1}^{N} Y_i} \cdot \frac{1}{1 - z^{-2}}$$

$$+ \frac{2 \cdot \sum_{i=2}^{N} Y_i \cdot \left(p_i \cdot z^{-1} - p_B \cdot z^{-2}\right)}{Y_B + \sum_{i=1}^{N} Y_i} \cdot \frac{1}{1 - z^{-2}}. \quad (31)$$

Solving (31) for p_B:

$$p_B = \frac{2 \cdot \left(\sum_{i=1}^{N} Y_i \cdot p_i\right) \cdot z^{-1}}{\left(Y_B + \sum_{i=1}^{N} Y_i\right) - \left(Y_B - \sum_{i=1}^{N} Y_i\right) \cdot z^{-2}}. \quad (32)$$

In the case of a boundary-node connected to an air-node in an otherwise homogeneous DWM system, with all admittances Y_i set such that they are equal to the admittance Y_1, the change in admittance at the boundary implies that if $Y_B = yY_1$ for $0 \leq y \leq 1$ where y is defined as in (8), (23) follows directly from (32).

These results, therefore, demonstrate the equivalence between an $M+1$ port K-DWM air-node connected directly to an N-port W-DWM boundary-node via a KW-pipe, the corresponding K-DWM formulation and, hence, by extension the equivalent W-DWM case. Note that the equivalent expressions (21), (27), and (32) are independent of air-node A1 and, hence, these results hold for any of the connecting terminals p_i (or

p_{N+j}) and, therefore, in turn hold for a W-DWM multiport boundary-node with up to N KW-pipe connected K-DWM air-nodes.

This result, therefore, completes the proof demonstrating that the KW-boundary hybrid termination is equivalent to either the K- or W-DWM case and, hence, is appropriate as a solution for DWM simulations that make use of efficient K-DWM air-nodes in combination with flexible W-DWM boundary-nodes without loss or error.

IV. TESTING AND EVALUATING THE HYBRID MESH

To test this new hybrid DWM based on K-DWM air-nodes and W-DWM/KW-boundary nodes, results are presented for the 2-D case. Ultimately, this work will be applied in the simulation of the acoustics of an enclosed space where large-scale, high resolution 3-D mesh structures will be a necessity. Hence, there is a need for hybrid DWM models that combine efficiency together with flexible boundary implementation. The examples presented here are based on 2-D geometries of a size and shape comparable to a horizontal plane through a typical room, although clearly they do not provide an accurate simulation of such a full 3-D system. Rather, these examples are presented as proof of principle to demonstrate the use of a hybrid DWM in a large-scale model, with a view to future implementation as part of a full 3-D DWM room modeling system. Some work has already been completed towards this goal [13]. Therefore, some of the terms used in the results as presented are those commonly found in room acoustics literature, although they are not strictly appropriate when considering the presented models as 2-D membranes. Prior work in DWM research often takes a similar approach to this problem, by establishing the 2-D case before moving to a full 3-D implementation, [15], [20]–[22], and large-scale 2-D models can also be used successfully for digital reverberation processing applications [3].

The results presented serve two purposes. First, to examine the computational improvements offered by the 2-D hybrid DWM over a standard W-DWM. Second, to present this new hybrid DWM in the context of a typical room modeling application by making use of interaural time difference (ITD) measurements obtained from binaural RIRs as an appropriate baseline reference. The improved geometrical flexibility of a triangular DWM at the boundary of a modeled space potentially offers an improvement in the accuracy of ITD measurements for binaural a RIR. However, DWMs based on the triangular six-port topology have a significant computational overhead when compared with a similar rectilinear model. The new hybrid DWMs presented help to alleviate this problem while still leaving the possibility for improved future boundary modeling solutions using W-model terminations.

A. Computational Improvements

Significant improvements are potentially offered by a hybrid mesh in terms of processing time and memory requirements over a standard W-DWM. A series of square 2-D meshes are simulated for a triangular W-DWM and a triangular KW-boundary hybrid DWM, each varying in surface area from 1 m^2 to 900 m^2 with $f_{update} = 44.1$ kHz. The simulations are performed on a standard PC with a 3.2-GHz P4 processor and
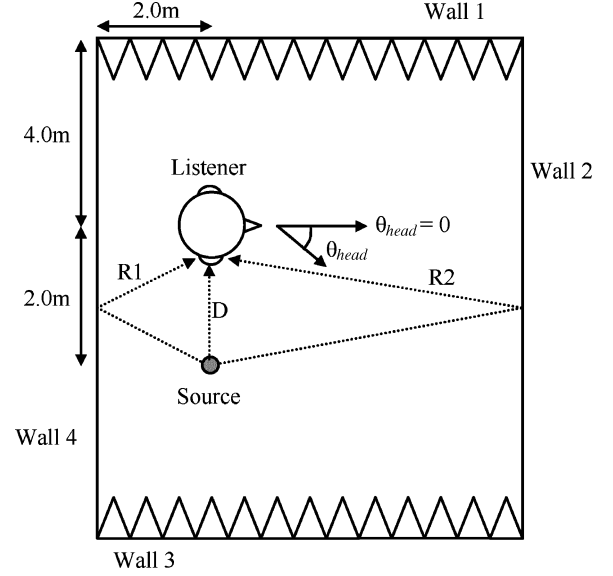

Fig. 8. A 9.0 × 5.0 m 2-D model for binaural RIR measurement using four different DWMs. Note that Walls 1 and 3 are defined as being anechoic.

1 GB of RAM and the time taken to process one output sample, and the total memory footprint for both cases are measured as a function of mesh size. The standard 2-D triangular W-DWM is used as the baseline measurement and in terms of memory use, a mesh size corresponding to an area of 900 m^2 requires 652 MB of RAM and takes 6.04 s to process one output sample. A processing speed increase of 34% and memory usage decrease of 50% is observed in the triangular hybrid DWM case for the same size mesh. These figures are typical as the size of the mesh varies over the individual simulation runs.

B. Binaural RIRs and ITD Measurements

This test scenario is designed to examine the potential spatial localization accuracy of the DWM due to its inherent diffraction and occlusion properties [3] and the advantages of the newly proposed triangular KW-boundary hybrid mesh. This involves adding a simple circular "head" to a 2-D model, and obtaining the RIRs at either side of this head at the position of the pinnae, allowing ITD effects to be measured. The path difference between a sound arriving at the ipsilateral ear via a straight line path, and the contralateral ear via an indirect path around a circular or spherical representation of the head can be calculated using geometrical ray-tracing techniques as, for instance, presented in [30]. From this path difference, an estimation of the ITD can be calculated.

A 2-D geometry of dimensions 9.0 × 5.0 m is defined as shown in Fig. 8. The circular head model of radius 0.09 m is placed as shown and two sets of binaural RIR measurements are made for $\theta_{head} = 0$ and, $\theta_{head} = \pi/2$. Walls 1 and 3 are defined as being anechoic, with Walls 2 and 4 being 100% reflective. This test scenario is investigated with four different 2-D mesh structures a follows:

1) rectilinear W-DWM;
2) triangular W-DWM;
3) triangular KW-boundary hybrid DWM;
4) triangular KW-boundary hybrid low memory (LM) DWM.

Case 1 is presented here as a benchmark against which the other triangular DWMs can be compared and so that the advantages of improved boundary-node connectivity can be highlighted. A full theoretical comparison of these two DWM topologies is beyond the scope of this paper but has been covered previously in some detail in [31]. In each case, the mesh sampling rate is fixed such that $f_{\text{update}} = 44.1$ kHz, giving the same internodal distance according to (6). The RIRs generated are resampled for analysis according to $0.25 \times f_{\text{update}}$ as would be the case in an auralization application, ensuring that the final bandwidth is valid and a fair comparison achieved.

Note that in Case 4, the triangular hybrid LM DWM algorithm has been optimized for low memory usage rather than speed of computation. In Case 3, each air-node data structure consists of three 32-bit pressure values for the current time pressure value and the previous two iterations, and six 32-bit pointers to the surrounding nodes giving a total memory use of 36 B per node. The pointers to the surrounding nodes are member variables, and will, hence, reside in the cache at the time of iteration implying that the required pressure values from surrounding nodes can be accessed quickly. In addition, no arrays are used, so CPU cycles are not wasted resolving a 3-D array into a single pointer, and the actual main iteration function does not require any additional parameters, so CPU cycles are again saved as there is no need to push and pop function arguments on and off the stack frame.

In Case 4, each air-node data structure again consists of three 32-bit pressure values for the current time pressure value and the previous two iterations, but no pointers to surrounding nodes are stored. Instead, these are supplied to each node when the main iteration function is called. As a result, these nodes only use 12 B of memory each but are executed more slowly as an array of six pointers to the surrounding nodes must first be resolved using indexing and a master array of node information.

The binaural RIRs for each of the four DWMs and for both values of θ_{head} are obtained, and ITDs are measured for the direct sound, D, and the first two reflections R1 and R2 as shown in Fig. 8. In addition, when measuring the binaural RIRs for D, Walls 2 and 4 are also defined as anechoic. Similarly, when considering R1, Wall 2 is set as anechoic, and when considering R2, Wall 4 is set as anechoic. This helps to minimize additional reflected components from surfaces not being examined in a particular case that may lead to errors in accurately determining ITD values. Note also that for case 1, the air-node coordinate positions (with the Wall 3/Wall 4 corner defined as the origin) for the left and right ears, respectively, are (272, 371) and (272, 354) for $\theta_{\text{head}} = 0$, and (264, 363) and (280, 363) for $\theta_{\text{head}} = \pi/2$. For cases 2–4, although different meshing algorithms are used due to the different underlying mesh structure, the left and right ear air-node coordinate positions are consistently set as (314, 371) and (314, 355) for $\theta_{\text{head}} = 0$, and (305, 363) and (323, 363) for $\theta_{\text{head}} = \pi/2$.

The ITD values from these measurements are calculated from the RIR pairs using cross-correlation and interpolated peak finding. No specific frequency weighting is applied as the geometrically calculated predicted values used for comparison are similarly not frequency dependent. The ITDs for the D cases are calculated directly. For R1 and R2, the direct components

TABLE II
BINAURAL RIR ITD MEASUREMENTS (IN ms) AND % ERROR

	$\theta_{head} = \pi/2$			$\theta_{head} = 0$		
	D	R1	R2	D	R1	R2
Predicted	0.0	0.529	0.579	0.680	0.230	0.168
Rectilinear W-DWM	0.0	0.643	0.713	0.821	0.284	0.192
(% Error)	*0.0*	*21.6*	*23.1*	*20.7*	*18.3*	*14.3*
Triangular W-DWM	0.0	0.627	0.702	0.797	0.275	0.191
(% Error)	*0.0*	*18.5*	*21.2*	*17.2*	*14.6*	*13.7*
Triangular Hybrid	0.0	0.629	0.701	0.799	0.272	0.19
(% Error)	*0.0*	*18.9*	*21.1*	*17.5*	*13.3*	*13.1*
Triangular Hybrid LM	0.0	0.629	0.701	0.799	0.272	0.19
(% Error)	*0.0*	*18.9*	*21.1*	*17.5*	*13.3*	*13.1*

TABLE III
COMPUTATIONAL REQUIREMENTS

	No. of Nodes	Memory Used (Mb)	Processing time (μs per sample per node)
Rectilinear W-DWM	371,735	22.739	0.224
Triangular W-DWM	429,450	30.909	0.257
Triangular Hybrid	429,450	15.751	0.222
Triangular Hybrid LM	429,450	6.575	0.388

are first removed from the RIRs by subtracting the appropriate D case, where all walls are defined as anechoic, and from the R1 and R2 cases, where only one wall is not anechoic. This ensures that the difference between RIRs is determined by the reflected component only. The comparative ITD results and percentage errors are summarized in Table II, with Table III presenting details relating to the computational load in terms of processing time and memory use for each DWM model.

From Table II it can be seen that the percentage errors for each ITD measurement are actually significant; however, they are also reasonably consistent across all cases. These relatively large errors, therefore, seem to indicate that the predicted values are a less than ideal first approximation to a true ITD measurement. However, despite this, the consistency of results demonstrates that they do serve for comparison purposes across model-types. In each case, moving from rectilinear W-DWM to triangular W-DWM shows a mean improvement in ITD measurement of 2.6% due to the additional connectivity options available at a boundary, facilitating a smoother fit to the circumference of the circular head model. The smallest improvement is evident for ($\theta_{\text{head}} = 0$, R2), being only 0.6%. This case also depends on the R2 wavefront traversing the smallest arc length around the circular head of all the examples presented. Therefore, the path difference between ears is less dependent on an accurate fit of the mesh to the head boundary and, hence, there is a correspondingly small improvement offered by a better fit

when moving from rectilinear to triangular mesh structure. As expected, both hybrid models result in exactly the same ITD values as the only variation between them is due to algorithm optimization. There is a slight variation between the two hybrid DWM models and the triangular W-DWM, and this is due to variations caused by the interpolated peak finding in the ITD calculation. If ITD values based on cross-correlation only are used then there is no difference between any of the triangular based DWM cases.

It is clear from Table III that although a 2-D triangular W-DWM requires approximately 16% more nodes than the 2-D rectilinear case, with an associated impact in terms of processing time and memory usage, the hybrid model offers a significant improvement over both, with the hybrid LM case making another significant saving in terms of memory used at the expense of processing time.

V. Conclusion

A new KW-boundary hybrid DWM has been presented and tested. The K-DWM 1-D N-port boundary-node termination has been shown to be equivalent to the W-DWM case and this leads to the KW-hybrid 1-D N-port boundary-node termination, shown to be equivalent to both the K- and W-DWM cases. In a particular example, this new KW-hybrid boundary-node has been implemented as part of a 2-D triangular DWM. This hybrid DWM has been tested in a number of simple 2-D applications and has been shown to demonstrate the improved geometrical flexibility of a standard triangular W-DWM at the boundary of a modeled space, resulting in improvements in the accuracy of ITD measurements for binaural RIRs. This is in addition to the significant computational savings that are made over standard W-DWM implementations in terms of memory use and processing time. The hybrid low memory DWM in particular would be useful for offline processing of large-scale 3-D DWMs in room acoustics applications, allowing the whole model to be computed from main system memory. With this new hybrid DWM established, future research will focus on the implementation of improved surface simulation through the use of further mixed modeling possibilities. This now includes the potential use of wave digital filters, which are considered in W-modeling terms [10], and the introduction of variable diffusively reflecting boundary conditions [23], as both offer computational compatibility with this new KW-boundary implementation.

Appendix

A. One-Dimensional Boundary Termination—K-DWM Derivation

The simplest 1-D termination of a DWM, as presented in Section III-A, considers a dummy junction connected on the other side of the boundary in question, essentially within the boundary itself—see Fig. 3. The dummy junction is connected to the boundary-node via waveguide admittance Y_B. The boundary-node in turn is connected to a single N-port scattering junction in the main body of the mesh (an air-node), with a waveguide element of admittance Y that is common to all lossless homogeneous waveguide elements in the structure.

The change in admittance from Y to Y_B defines the reflection coefficient r

$$r = \frac{Y - Y_B}{Y + Y_B} \tag{A1}$$

where $0 \leq r \leq 1$. If $Y_B = yY$ for $0 \leq y \leq 1$, then

$$y = \frac{1-r}{1+r} \tag{A2}$$

Given that there is no contribution into the boundary-node B from the dummy junction D, the sound pressure for the boundary-node can be calculated, as presented in (9), as a function of the sound pressures of the incident traveling waves

$$p_B = (1+r) \cdot p_{B,1}^+. \tag{A3}$$

Substituting (A3) in (2) and rearranging for $p_{B,1}^-$ gives the outgoing pressure wave from the boundary-node to the air-node

$$p_{B,1}^- = r \cdot p_{B,1}^+. \tag{A4}$$

Now, considering again the sound pressure at boundary-node B from (3), and noting that there is no contribution from the dummy junction D, gives

$$p_B = \frac{2 \cdot Y \cdot p_{B,1}^+}{Y + y \cdot Y}. \tag{A5}$$

Eliminating the common factor Y and rearranging

$$p_{B,1}^+ = \frac{1}{2} p_B \cdot (1+y). \tag{A6}$$

Now, by considering Fig. 3 and from (4)

$$p_{B,1}^+ = p_{1,B}^- \cdot z^{-1}. \tag{A7}$$

Further, considering the z-transform of (2), the right hand side of (A7) can be expressed as

$$p_{1,B}^- \cdot z^{-1} = p_1 \cdot z^{-1} - p_{1,B}^+ \cdot z^{-1}. \tag{A8}$$

Note that from (4), the last term in (A8) can be expressed as

$$p_{1,B}^+ \cdot z^{-1} = p_{B,1}^- \cdot z^{-2}. \tag{A9}$$

Substituting (A4) in (A9)

$$p_{1,B}^+ \cdot z^{-1} = r \cdot p_{B,1}^+ \cdot z^{-2}. \tag{A10}$$

Now it is possible to substitute (A6) into (A10)

$$p_{1,B}^+ \cdot z^{-1} = \frac{r}{2} \cdot p_B \cdot (1+y) \cdot z^{-2}. \tag{A11}$$

Equating (A7) and (A8) and substituting (A11) in (A8) gives an expression for the pressure signal incident on boundary-node B from air-node 1 in terms of node pressure values only

$$p_{B,1}^+ = p_1 \cdot z^{-1} - \left[\frac{r}{2} \cdot p_B \cdot (1+y) \cdot z^{-2} \right]. \tag{A12}$$

Substituting (A12) in (A5)

$$p_B = \left(\frac{2}{1+y}\right)\left\{p_1 \cdot z^{-1} - \left[\frac{r}{2} \cdot p_B \cdot (1+y) \cdot z^{-2}\right]\right\}. \tag{A13}$$

Simplifying

$$p_B = \left(\frac{2 \cdot p_1 \cdot z^{-1}}{1+y}\right) - r \cdot p_B \cdot z^{-2}. \tag{A14}$$

Finally, substituting (A2) in (A14) gives

$$p_B = (1+r)p_1 \cdot z^{-1} - r \cdot p_B \cdot z^{-2}. \tag{A15}$$

Equation (A15), as also presented in (10), is therefore the K-model formulation of a 1-D boundary termination in a DWM, determined by the reflection factor r, with $r = 1$ giving total reflection and $r = 0$ approximating anechoic conditions.

REFERENCES

[1] S. A. Van Duyne and J. O. Smith, "Physical modeling with the 2-D digital waveguide mesh," in *Proc. Int. Comput. Music Conf.*, Tokyo, Japan, 1993, pp. 40–47.

[2] L. Savioja, T. J. Rinne, and T. Takala, "Simulation of room acoustics with a 3-D finite difference mesh," in *Proc. Int. Comput. Music Conf.*, Aarhus, Denmark, 1994, pp. 463–466.

[3] D. T. Murphy and M. J. Beeson, "Modeling spatial sound occlusion and diffraction effects with the digital waveguide mesh," in *Proc. Audio Eng. Soc. 24th Int. Conf.*, Banff, Canada, Jun. 26–28, 2003, pp. 207–216.

[4] U. Stephenson, "Comparison of the image source method & the particle simulation method," *Appl. Acoust.*, no. 29, pp. 35–72, 1990.

[5] A. Farina, "Pyramid tracing vs. ray tracing for the simulation of sound propagation in large rooms," in *Computational Acoustics & Its Environmental Applications*. Southampton, U.K.: Computational Mechanics, 1995, pp. 109–116.

[6] N. Tsingos, T. Funkhouser, A. Ngan, and I. Carlbom, "Modeling acoustics in virtual environments using the uniform theory of diffraction," in *Proc. SIGGRAPH*, Los Angeles, CA, Aug. 12–17, 2001, pp. 545–552.

[7] J. R. Wright, "An exact model of acoustic radiation in enclosed spaces," *J. Audio Eng. Soc.*, vol. 43, no. 5, pp. 813–820, Oct. 1995.

[8] J. O. Smith, "Physical modeling using digital waveguides," *Comput. Music J.*, vol. 16, no. 4, pp. 74–87, Winter 1992.

[9] J. L. Kelly and C. C. Lochbaum, "Speech synthesis," in *Proc. 4th Int. Congr. Acoust.*, Copenhagen, Denmark, Sep. 1962, pp. 1–4.

[10] M. Karjalainen and C. Erkut, "Digital waveguides versus finite difference structures: Equivalence and mixed modeling," *EURASIP J. Appl. Signal Process.*, vol. 7, pp. 978–989, Jun. 2004.

[11] C. Erkut and M. Karjalainen, "Finite difference method vs. digital waveguide method in string instrument modeling and synthesis," in *Proc. ISMA*, Mexico City, Mexico, Dec. 9–13, 2002, (CD-ROM).

[12] J. O. Smith, On the Equivalence of Digital Waveguide and Finite Difference Time Domain Schemes, arXiv:physics/0407032 v4, Jul. 27, 2004 [Online]. Available: http://arxiv.org/abs/physics/0407032/

[13] M. J. Beeson and D. T. Murphy, "RoomWeaver: A digital waveguide mesh based room acoustics research tool," in *Proc. of 7th Int. Conf. Digital Audio Effects (DAFX-04)*, Naples, Italy, Oct. 5–8, 2004, pp. 268–273.

[14] J. O. Smith, "Principles of digital waveguide models of musical instruments," in *Applications of Digital Signal Processing to Audio and Acoustics*, M. Kahrs and K. Brandenburg, Eds. Boston, MA: Kluwer, 1998, pp. 417–466.

[15] J. Mullen, D. T. Murphy, and D. M. Howard, "Digital waveguide mesh modeling of the vocal tract acoustics," in *Proc. IEEE Workshop Applications Signal Process. Audio Acoust.*, New Paltz, NY, Oct. 19–22, 2003, pp. 163–168.

[16] F. Fontana and D. Rocchesso, "A new formulation of the 2-D waveguide mesh for percussion instruments," in *Proc. XI Colloq. Musical Informatics*, Bologna, Italy, Nov. 1995, pp. 27–30.

[17] L. Savioja, J. Backman, A. Järvinen, and T. Takala, "Waveguide mesh method for low-frequency simulation of room acoustics," in *Proc. Int. Congr. Acoust.*, Trondheim, Norway, Jun. 26–30, 1995, vol. 2, pp. 637–641.

[18] S. A. Van Duyne and J. O. Smith, III, "The 3-D tetrahedral digital waveguide mesh with musical applications," in *Proc. Int. Comput. Music Conf.*, Hong Kong, 1996, pp. 9–16.

[19] F. Fontana, D. Rocchesso, and E. Apollonio, "Using the waveguide mesh in modeling 3-D resonators," in *Proc. of DAFX-00*, Verona, Italy, Dec. 7–9, 2000, pp. 229–232 [Online]. Available: http://profs.sci.univr.it/~dafx/DAFx-final-papers.html

[20] L. Savioja and V. Välimäki, "Reducing the dispersion error in the digital waveguide mesh using interpolation and frequency warping techniques," *IEEE Trans. Speech Audio Process.*, vol. 8, no. 2, pp. 184–194, Mar. 2000.

[21] ——, "Interpolated rectangular 3-D digital waveguide mesh algorithms with frequency warping," *IEEE Trans. Speech Audio Process.*, vol. 11, no. 6, pp. 783–789, Nov. 2003.

[22] A. Kelloniemi, D. T. Murphy, L. Savioja, and V. Välimäki, "Boundary conditions in a multi-dimensional digital waveguide mesh," in *Proc. IEEE ICASSP*, Montreal, QC, Canada, May 17–21, 2004, pp. IV-25–IV-28.

[23] S. Shelley and D. T. Murphy, "Measuring diffusion in a 2-D digital waveguide mesh," in *Proc. DAFX-05*, Madrid, Spain, Sep. 20–22, 2005 [Online]. Available: http://dafx05.ssr.upm.es/Proc_DAFx05/P_249.pdf

[24] S. A. Van Duyne and J. O. Smith, "A simplified approach to modeling dispersion caused by stiffness in strings and plates," in *Proc. Int. Comput. Music Conf.*, Århus, Denmark, 1994, pp. 407–410.

[25] J. Laird, P. Masri, and C. N. Canagarajah, "Modeling diffusion at the boundary of a digital waveguide mesh," in *Proc. Int. Comput. Music Conf.*, Beijing, China, 1999, pp. 492–495.

[26] F. Fontana, "Physics-Based Models for the Acoustic Representation of Space in Virtual Environments" Ph.D. dissertation, Dept. Comput. Sci., Univ. Verona, Verona, Italy, Apr. 2003 [Online]. Available: http://profs.sci.univr.it/~fontana/paper/20.pdf

[27] L. Savioja, M. Karjalainen, and T. Takala, "DSP formulation of a finite difference method for room acoustics simulation," in *Proc. IEEE Nordic Signal Process. Symp. (NORSIG'96)*, Espoo, Finland, Sep. 24–27, 1996, pp. 455–458.

[28] J. Huopaniemi, L. Savioja, and M. Karjalainen, "Modeling of reflections and air absorption in acoustical spaces: A digital filter design approach," in *Proc. IEEE Workshop Applications Signal Process. Audio Acoust. (WASPAA'97)*, New Paltz, NY, Oct. 19–22, 1997 [Online]. Available: http://www.acoustics.hut.fi/~ruba/pubs/refair.ps

[29] T. I. Laakso, V. Välimä, M. Karjalainen, and U. K. Laine, "Splitting the unit delay—tools for fractional delay filter design," *IEEE Signal Process. Mag.*, vol. 13, no. 1, pp. 30–60, Jan. 1996.

[30] H. Sowizral, K. Rushforth, and M. Deering, *The Java 3-D API Specification*. Reading, MA: Addison Wesley, 2000.

[31] F. Fontana and D. Rocchesso, "Signal-theoretic characterization of waveguide mesh geometries for models of two-dimensional wave propagation in elastic media," *IEEE Trans. Speech Audio Process.*, vol. 9, no. 2, pp. 152–161, Feb. 2001.

Damian T. Murphy received the B.Sc. (Hons) degree in mathematics in 1993, the M.Sc. degree in music technology in 1995, and the D.Phil. degree in music technology in 2000, all from the University of York, York, U.K.

In 1999 he was Lecturer in Music Technology in the School of Engineering, Leeds Metropolitan University, Leeds, U.K., and in 2000 was appointed as Lecturer in the Department of Electronics, University of York. He has worked as an Audio Consultant and since 2002 has been a Visiting Lecturer in the Department of Speech, Music, and Hearing, KTH, Stockholm, Sweden. His research is in the areas of physical modeling and spatial sound, with particular interests in applications of the digital waveguide mesh. He is an active composer in the fields of electroacoustic and electronic music, where sound spatialization forms a critical aspect of his musical works.

Dr. Murphy is a member of the Audio Engineering Society. In 2004, he was appointed as one of the U.K.'s first AHRC/ACE Arts and Science Research Fellows, investigating the compositional and aesthetic aspects of sound spatialization and acoustic modeling techniques.

Mark Beeson received the first class M.Eng. degree in electronic engineering and music technology systems from the University of York, York, U.K., in 2002.

He has worked as an Audio Consultant and Programmer specializing in audio for mobile devices and was appointed to the Department of Electronics, University of York, in January 2003. He was also a Visiting Researcher at the Department of Speech, Music, and Hearing, KTH, Stockholm, Sweden, from July to October 2004. His research interests are in the areas of virtual acoustics and applications of the digital waveguide mesh, and he is the lead developer of the RoomWeaver digital waveguide mesh room acoustics modeling software.